doi: 10.18323/2782-4039-2024-3-69-7

Microstructure, crystallographic texture and mechanical properties of the Zn–1%Mg–1%Fe alloy subjected to severe plastic deformation

Vil D. Sitdikov*[1,2,4], Doctor of Sciences (Physics and Mathematics), senior expert, senior researcher
Elvira D. Khafizova[2,3,5], PhD (Engineering), assistant professor of Chair of Materials Science and Metal Physics, senior researcher at the Research Laboratory "Metals and Alloys under Extreme Exposures"
Milena V. Polenok[2,3,6], graduate student of Chair of Materials Science and Physics of Metals, research assistant at the Research Laboratory "Metals and Alloys under Extreme Exposures"
[1]*OOO RN-BashNIPIneft, Ufa (Russia)*
[2]*Institute of Physics of Molecules and Crystals of Ufa Federal Research Center of RAS, Ufa (Russia)*
[3]*Ufa University of Science and Technology, Ufa (Russia)*

***E-mail:** SitdikovVD@bnipi.rosneft.ru

[4]ORCID: https://orcid.org/0000-0002-9948-1099
[5]ORCID: https://orcid.org/0000-0002-4618-412X
[6]ORCID: https://orcid.org/0000-0001-9774-1689

Received 09.02.2024 *Accepted 19.07.2024*

Abstract: The paper covers the production, analysis of the microstructure, crystallographic texture and deformation mechanisms of the ultrafine-grained (UFG) Zn–1%Mg–1%Fe zinc alloy demonstrating unique physical and mechanical properties compared to its coarse-crystalline analogs. The zinc alloy with improved mechanical properties was developed in two stages. At the first stage, based on the analysis of literature data, an alloy with the following chemical composition was cast: Zn–1%Mg–1%Fe. Then, the alloy was subjected to high-pressure torsion (HPT) to improve mechanical properties due to grain structure refinement and implementation of dynamic strain aging. The conducted mechanical tensile tests of the samples and assessment of the alloy hardness showed that HPT treatment leads to an increase in its tensile strength to 415 MPa, an increase in hardness to 144 HV, and an increase in ductility to 82 %. The obtained mechanical characteristics demonstrate the suitability of using the developed alloy in medicine as some implants (stents) requiring high applied loads. To explain the reasons for the improvement of the mechanical properties of this alloy, the authors carried out comprehensive tests using microscopy and X-ray diffraction analysis. The microstructure analysis showed that during the formation of the ultrafine-grained structure, a phase transition is implemented according to the following scheme: $Zn_{eutectic} + Mg_2Zn_{11eutectic} + FeZn_{13} \rightarrow Zn_{phase} + Mg_2Zn_{11phase} + MgZn_{2particles} + Zn_{particles}$. It was found that as a result of high pressure torsion in the main phases (Zn, Mg_2Zn_{11}), the grain structure is refined, the density of introduced defects increases, and a developed crystallographic texture consisting of basic, pyramidal, prismatic, and twin texture components is formed. The study showed that the resistance of pyramidal, prismatic and twin texture components at the initial stages of high-pressure torsion determines the level and anisotropy of the strength properties of this alloy. The relationship between the discovered structural features of the produced alloy and its unique mechanical properties is discussed.

Keywords: Zn–1%Mg–1%Fe alloy; phase transformations in zinc alloy; severe plastic deformation; X-ray scattering methods; mechanical properties; strength; ductility; crystallographic texture.

Acknowledgements: The study was funded by the grant of the Russian Science Foundation No. 23-29-00667, https://rscf.ru/project/23-29-00667.

For citation: Sitdikov V.D., Khafizova E.D., Polenok M.V. Microstructure, crystallographic texture and mechanical properties of the Zn–1%Mg–1%Fe alloy subjected to severe plastic deformation. *Frontier Materials & Technologies*, 2024, no. 3, pp. 75–88. DOI: 10.18323/2782-4039-2024-3-69-7.

INTRODUCTION

Zinc alloys belong to a new class of biodegradable materials, that demonstrate excellent biocompatibility and biodegradability along with relatively high mechanical strength and sufficient ductility [1–4]. According to the literature, the initial pure zinc is a very brittle material, and its low mechanical properties (yield strength ~10 MPa, tensile strength ~18 MPa, ductility 0.3 %) limit its scope of industrial application [5; 6]. To increase the potential for industrial application of zinc, for example, as implants in medicine, it is necessary to optimise its physical and mechanical properties [1–4]. Traditionally, this goal is achieved by alloying pure zinc with certain atoms (Mg, Li, Ca, Fe, Mn, Ag, Cu, etc.), and performing thermomechanical treatment [1–4]. However, most zinc alloys produced in this way, suitable for implants, may contain elements toxic to the human body. In this regard, the scientific community is still searching for new materials that, on the one hand, should meet the desired mechanical characteristics for implants, and on the other hand, be biocompatible.

As is known, when developing biodegradable implants from various alloys, it is necessary to control the corrosion rate, since at high rates, the mechanical integrity of the implants is disrupted before the bone heals, and at too slow corrosion rate, inflammatory processes can be activated [7–9]. Clinical studies have shown that in Zn–xAl system implants, the risk of an inflammatory reaction increases [10], and alloying zinc with Fe atoms significantly reduces it [11]. As is known, Fe is one of the most important elements in the human body, but excessive addition of Fe to Zn leads to the formation of a brittle $FeZn_{13}$ phase, which worsens the mechanical characteristics of Zn–Fe alloys [12]. On the other hand, adding a certain amount of Mg atoms can also strengthen the Zn phase, but the strength and ductility of the resulting Zn–Mg alloys still remain relatively low [13]. In particular, the authors of [13] showed that the ultimate tensile strength of the Zn–Mg alloy can increase to 125 MPa with an increase in the Mg content from 0.1 to 0.8 %, however, the ductility of the resulting alloy remains low (less than 1 %). With a further increase in the Mg content in the alloy to 3.0 %, it is possible to achieve an increase in the ultimate tensile strength to ~150 MPa, and the elongation before failure increases to only 2 % [14; 15]. Moreover, studies have shown that an increase in the Mg content in Zn also leads to an increase in the hardness of the obtained alloy [11; 16]. In particular, it was demonstrated that adding 1 wt. % of Mg to pure Zn, leads to an increase in its hardness from 40 to 78 HV according to the Vickers scale [16], and in [11], the authors have shown that the hardness of the Zn–1.3%Fe alloy can reach 56 HV.

The conducted literature analysis revealed that the Zn–Mg–Fe system alloys can be used to produce zinc alloys with increased strength and biocompatibility in medicine. In this regard, Mg and Fe were also chosen as alloying elements in this work to create a zinc alloy with an improved structure. The choice of these elements was also influenced by the fact, that the solubility rate of Zn in the body is between the solubility rates of Mg and Fe, and the degradation products are biocompatible [2; 7–9]. Moreover, the authors of [17], as a result of varying the degree of alloying of zinc with Mg and Fe atoms, found that the Zn–1%Mg–1%Fe alloy, compared to other Mg and Fe contents in zinc, shows the highest strength properties (ultimate tensile strength σ_{UTS} is 157 MPa, yield strength σ_y is 148 Mpa), and an acceptable corrosion rate (0.027 mm/year). However, the ductility δ of the produced alloy was low (no more than 2.3 %) [17]. Nevertheless, the improved mechanical properties, satisfactory corrosion rate and biocompatibility of the coarse-grained Zn–1%Mg–1%Fe alloy became the basis for the authors of this work to choose this alloy for further optimisation of its strength characteristics and ductility, so that it meets the required criteria for implants (σ_{UTS}>300 MPa, σ_y>200 MPa, δ>15 %) [2]. In this case, the authors of this work optimised the mechanical properties of Zn–1%Mg–1%Fe using the method of severe plastic deformation (SPD) [18].

Recently, a number of studies [19; 20] have shown that SPD methods can more effectively increase the strength characteristics of zinc alloys by forming an ultrafine-grained (UFG) structure, increasing the defectiveness of the structure, and implementing the process of dynamic deformation ageing, during which the strengthening phases of the particle precipitate. At the same time, improving the above-mentioned microstructure parameters, leading to an increase in the mechanical properties of zinc alloys, is possible, due to variations in the applied pressure, temperature, and degree of SPD. In this regard, in this work, improving the mechanical properties of the cast Zn–Mg–Fe alloy was also achieved by optimising the modes (pressure, temperature, deformation degree), of high-pressure torsion (HPT) [18; 19].

The aim of this work is, using high-pressure torsion processing, to produce an ultrafine-grained Zn–1%Mg–1%Fe zinc alloy, demonstrating the required mechanical properties for application as implants (stents) in medicine.

METHODS

Cylindrical specimens of Zn–1%Mg–1%Fe alloy (mass percent), with a diameter of 20 mm and a length of 120 mm were cast from high-purity Zn (>99.9 wt. %), Mg (>99.9 wt. %) and Fe (>99.9 wt. %) at a temperature of 600 °C in a chamber furnace using a graphite crucible. To form a UFG structure in order to improve the strength characteristics, tablets (radius R is 10 mm, thickness is 1.7 mm) of the alloy, cut from cylindrical specimens, were subjected to HPT at room temperature (27 °C), and at a temperature of 150 °C, varying the number of revolutions from 0.5 to 10. After each stage of HPT, corresponding to 0.5; 1; 2; 3; 6; 8 and 10 revolutions of the lower striker (the deformation degree γ corresponds to 28.5; 57.1; 114.2; 171.3; 342.6; 456.8 and 571.0 for the $R/2$ region, according to [18]), the authors analysed the mechanical properties and microstructure of the alloy. The applied hydrostatic pressure during HPT was 6 GPa, the striker rotation rate was set at 1 rpm. Mechanical tensile tests of the alloy were performed, using a specialised testing machine, for small samples (length of the working part is 4 mm, thickness is 1 mm, width is 1 mm). The working part of the tensile samples was located in the area, which was at half the radius of the disk-shaped HPT sample. The frequency of digitising of the deformation values when recording the tensile curves, during continuous testing of the samples was set to 4 Hz. The traverse speed was $4 \cdot 10^{-4}$ mm/s. The microhardness of the alloy, in each structural state, was measured by the Vickers method on a universal Shimadzu HMV-G hardness tester (Japan), with an indenter load of 100 g. The measurements were performed in the area located at half the radius of the disk-shaped HPT sample.

The fine structure parameters of the alloy, were determined by X-ray diffraction analysis (XRD). The XRD diffraction patterns were measured on a Bruker D8 Advance diffractometer (Germany) (Bragg–Brentano scheme). The shooting was carried out in the continuous shooting mode, at a rate of 1.5 °/min within the scattering angle 2θ from 20 to 150°, on copper radiation generated at a voltage of 40 kV and a current of 40 mA. Pulse counting was performed using a LinxEye multichannel detector (Germany). A Ni filter was installed in front of the detector to cut off

unnecessary radiation. The lattice constant was estimated, the average size of the coherent scattering domains (CSD) was determined, and the dislocation density was calculated using the PM2K program [21].

Qualitative X-ray phase analysis was performed, using the PDF-2 diffraction database using the EVAplus program (www.bruker.com). Quantitative X-ray phase analysis, with identifying the ratio of the detected phases, was performed applying the Rietveld method [22] using the TOPAS program, ver. 4.2 (www.bruker.com). In this algorithm, the atomic-structural parameters of all detected phases are input into the model, and the theoretical diffraction pattern is reproduced. For the best approximation of the theoretical $I_{measured}$ curve to the experimental $I_{calculated}$, the fine structure parameters (lattice constant, microstrain, crystallite size, and crystallographic texture) are optimised, taking into account possible errors made during shooting. The microstructure of the alloy under study was analysed by scanning electron microscopy (SEM), using an FEI Thermo Scientific Q250 scanning electron microscope (USA). The main shooting characteristics were: electron accelerating voltage – 25 kV, beam diameter – 2 μm, focal length – 10.0 mm, chamber pressure – $5 \cdot 10^{-4}$ Pa. Microstructure studies using X-ray diffraction and SEM were conducted in the areas where mechanical tests were performed.

RESULTS

The results of mechanical tests of the Zn–1%Mg–1%Fe alloy in different structural states, showed that HPT treatment (except for microhardness at HPT 27 °C) leads to an increase in its strength characteristics (Table 1). In particular, in the initial state, the Vickers microhardness of the alloy did not exceed 118 HV. At the same time, the application of 1 revolution of HPT treatment to the alloy at room temperature, led to a decrease in the microhardness to 114 HV. With a subsequent increase in the degree of HPT treatment to 6 revolutions, the microhardness of the alloy naturally drops to 109 HV. At high degrees of deformation (10 revolutions), the microhardness of the studied alloy remains virtually unchanged. However, with an increase in the temperature of the HPT treatment (1 revolution, 150 °C), on the contrary, even at the initial stages, a regular increase in microhardness to 131 HV is observed (Table 1). With a further increase in the number of revolutions of the HPT treatment, the alloy demonstrates a slight decrease in its microhardness (Table 1).

The results of mechanical tensile tests of the alloy are also summarised in Table 1. In general, the analysis of Table 1 indicates that the implementation of HPT treatment even at the initial stages of processing (27 °C) leads to an increase in the alloy strength and ductility. In particular, after 1 HPT revolution, an increase in the ultimate tensile strength to 289 MPa is observed, and the ductility reaches 95 %. As the number of HPT revolutions increases to 6, the yield strength and ultimate tensile strength of the alloy slightly decrease, and the level of ductility is maintained. With high degrees of HPT treatment, implemented at room temperature, the strength characteristics increase again, but the ductility of the alloy decreases noticeably. On the other hand, increasing the HPT temperature (150 °C) leads to an increase in both the hardness value, and the values of the ultimate tensile strength and ductility of the alloy. Thus, after 1 HPT revolution, the ultimate tensile strength increases to 399 MPa, which is 110 MPa more than that obtained after 1 HPT (27 °C) revolution. After 3 HPT (150 °C) revolutions, a further increase in the ultimate

Table 1. *The values of microhardness and mechanical properties of the Zn–1%Mg–1%Fe alloy*
Таблица 1. *Значения микротвердости и механических свойств сплава Zn–1%Mg–1%Fe*

State		HV	σ_y, MPa	σ_{UTS}, MPa	δ, %
Initial		**118 ± 3**	**28 ± 2**	**33 ± 3**	**6 ± 1**
HPT 27 °C	1 rev.	114 ± 4	213 ± 12	289 ± 11	95 ± 5
	3 rev.	112 ± 4	189 ± 10	271 ± 9	96 ± 4
	6 rev.	109 ± 3	177 ± 9	255 ± 12	97 ± 6
	10 rev.	110 ± 4	191 ± 8	264 ± 11	61 ± 5
HPT 150 °C	1 rev.	131 ± 4	313 ± 13	399 ± 15	85 ± 6
	3 rev.	129 ± 3	312 ± 14	415 ± 10	82 ± 4
	6 rev.	126 ± 5	307 ± 9	394 ± 13	86 ± 5
	10 rev.	128 ± 4	304 ± 10	387 ± 14	89 ± 6

Note. HV is Vickers microhardness; σ_y is yield stress; σ_{UTS} is ultimate tensile strength; δ is percent elongation to fracture.
Примечание. HV – величина микротвердости по Виккерсу; σ_y – предел текучести; σ_{UTS} – предел прочности; δ – относительное удлинение до разрушения.

tensile strength value is observed (up to 415 MPa), with maintaining the ductility level. With a subsequent increase in the HPT degree, the alloy strength characteristics decrease slightly, and its ductility increases slightly (Table 1). In general, the mechanical tests showed that at the initial stages of HPT treatment (1–3 revolutions), at a temperature of 150 °C, the zinc alloy demonstrates high strength characteristics with sufficient ductility (Table 1).

Fig. 1 shows the SEM images of the initial zinc alloy microstructure, as well as the results of the surface distribution of Zn, Mg and Fe atoms over a random area of the polished section. According to the phase diagram of Zn–Mg [23] and Zn–Fe [24], the phases of Zn, Mg_2Zn_{11} and $FeZn_{13}$ should be present in the cast Zn–1%Mg–1%Fe alloy. In fact, the data obtained by SEM and X-ray phase analysis (data are given below) showed that the microstructure of the studied alloy contains the Zn, Mg_2Zn_{11} and $FeZn_{13}$ phases (Fig. 1 a). In this case, according to the SEM data, the Mg_2Zn_{11} phase is concentrated at the boundaries of the zinc phase (Fig. 1 a).

Since the atomic mass of Zn is greater than the atomic mass of Mg, the relatively light oval-shaped areas belong to the zinc phase, and the dark areas correspond to the Mg_2Zn_{11} phase (Fig. 1 a). The analysis of the microstructure by the elemental mapping method factually confirms the above-detected shape, and nature of occurrence of the phases identified in the alloy (Fig. 1 b). Calculations showed that the average grain diameter of the Zn phase is 88 μm, and the size of the $FeZn_{13}$ phase varies from 1.5 to 280 μm (Fig. 1 a, 1 b).

Fig. 2 shows SEM images of the microstructure of the studied alloy after heat treatment (150 °C), and HPT processing carried out at different temperatures (27 and 150 °C). After heat treatment, the alloy microstructure contains Zn, Mg_2Zn_{11} and $FeZn_{13}$ phases. These phases are marked with arrows in Fig. 2 a. It is also evident that cylindrical $MgZn_2$ particles precipitate in the Mg_2Zn_{11} phase (dark area) as a result of heat treatment (Fig. 1 a, inset). We should note that in the cast state, $MgZn_2$ particles in the Mg_2Zn_{11} phase were not detected.

In the case of HPT treatment, even with a small rotation of the anvils (0.5 revolution), noticeable changes in the microstructure of the analysed alloy can be observed (Fig. 2 b). These changes are mainly related to the fact that a band structure of alternating Mg_2Zn_{11}, Zn and $FeZn_{13}$ phases is formed in the alloy (Fig. 2 b). Moreover, HPT treatment led to the fragmentation of $FeZn_{13}$ phase grains, as well as a change in the shape and size of particles that precipitated during annealing, ($MgZn_2$ particles in the Mg_2Zn_{11} phase) (Fig. 2 b, in the inset). With an increase in the number of HPT revolutions, i.e. the degree of deformation, both a decrease in the width of the bands of the observed phases, and a further refinement of the grains of each phase are observed. In particular, a typical microstructure of the alloy after 6 revolutions of HPT treatment is shown in Fig. 2 c. For clarity, this microstructure is presented as a distribution map of the Zn, Mg and Fe elements (Fig. 2 c). It is evident that in this state of the alloy, the band structure consisting of Zn (green areas), Mg_2Zn_{11} (blue areas) and $FeZn_{13}$ (red areas) phases is maintained. In contrast to the early HPT stages, after 6 revolutions, a significant refinement of the grain structure is observed in the Mg_2Zn_{11} phase (Fig. 2 c, in the inset). According to microscopy data, the average grain size of the Mg_2Zn_{11} phase was 320 nm.

At high degrees of HPT treatment (10 revolutions), the alloy is characterised by a decrease in the thickness of the bands corresponding to the Zn and Mg_2Zn_{11} phases (Fig. 2 d). Further refinement of the structure components is observed in these bands (Fig. 2 d). In particular, in this state, the grains of the Mg_2Zn_{11} phase are also characterised by an equiaxial structure, but the average grain size decreases to 230 nm. The analysis showed that at high HPT revolutions, precipitated Zn and $MgZn_2$ particles of spherical morphology could be randomly observed in the Mg_2Zn_{11} phase (Fig. 2 d, inset).

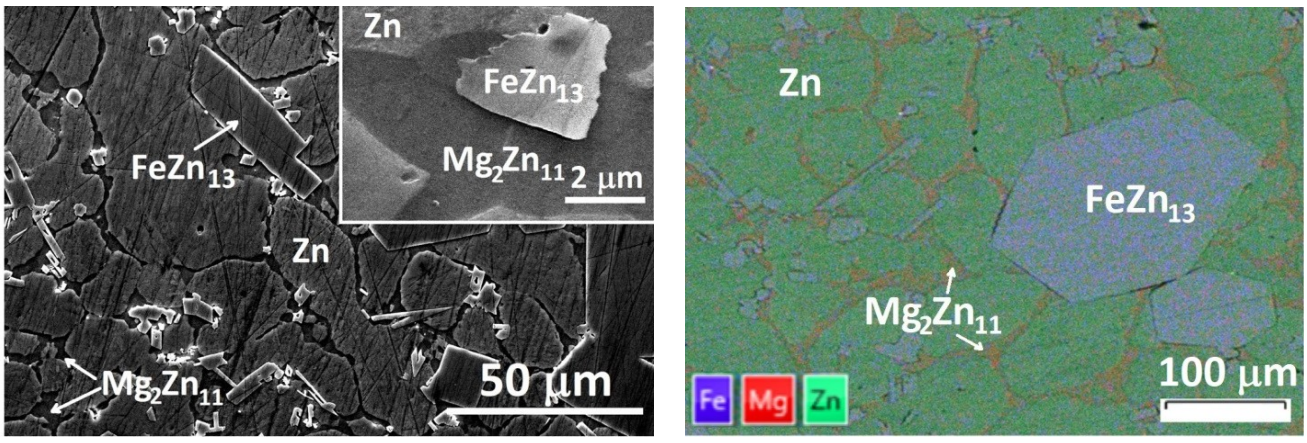

a *b*

Fig. 1. *Microstructure of the Zn–1%Mg–1%Fe alloy (in a random area of the section) in initial (as-cast) state:* ***a*** *– image at ×2400 magnification;* ***b*** *– image of the distribution of Zn, Mg and Fe atoms at ×500 magnification*

Рис. 1. *Микроструктура Zn–1%Mg–1%Fe сплава (в произвольном участке шлифа) в исходном (литом) состоянии:* ***a*** *– изображение при увеличении ×2400;* ***b*** *– изображение распределения атомов Zn, Mg и Fe при увеличении ×500*

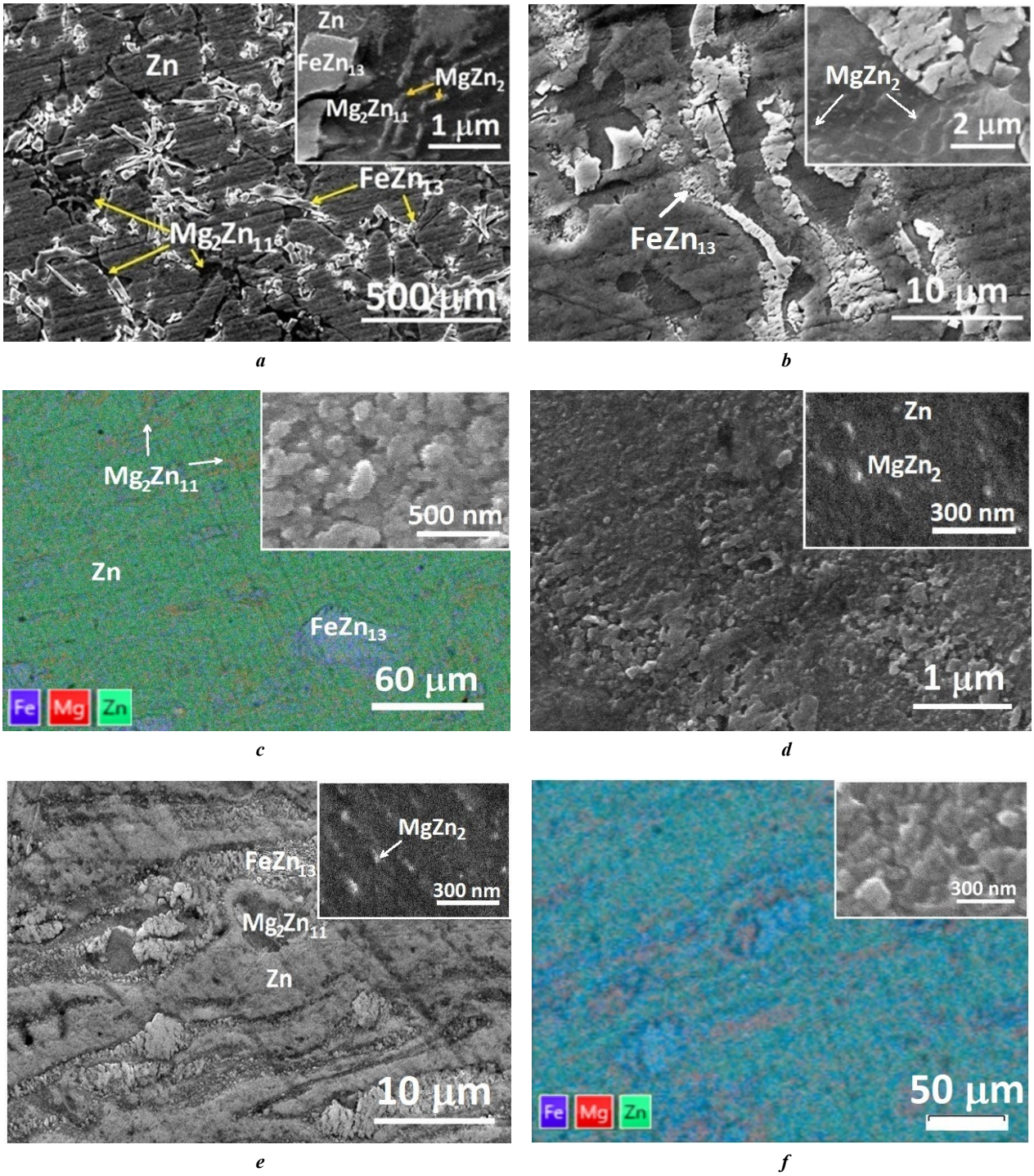

Fig. 2. *Microstructure of the Zn–1%Mg–1%Fe alloy in different structural states:* ***a*** *– after heat treatment;* ***b*** *– after 0.5 rev. of HPT 27 °C;* ***c*** *– after 6 rev. of HPT 27 °C;* ***d*** *– after 10 rev. of HPT 27 °C;* ***e*** *– after 1 rev. of HPT 150 °C;* ***f*** *– after 3 rev. of HPT 150 °C*

Рис. 2. *Микроструктура Zn–1%Mg–1%Fe сплава в различных структурных состояниях:* ***a*** *– после термической обработки;* ***b*** *– после 0,5 об. ИПДК 27 °C;* ***c*** *– после 6 об. ИПДК 27 °C;* ***d*** *– после 10 об. ИПДК 27 °C;* ***e*** *– после 1 об. ИПДК 150 °C;* ***f*** *– после 3 об. ИПДК 150 °C*

When conducting HPT treatment of the alloy at an elevated temperature (150 °C), a banded structure is formed even after 1 revolution (Fig. 2 e). The average thickness of the Mg_2Zn_{11} phase plates in this state is 2.9 μm, and inside the plates, the average size of equiaxial grains is 362 nm. A similar structure is observed when implementing high degrees of HPT in the alloy at room temperature. With an increase in the HPT degree, the thickness of the Zn and $MgZn_2$ phase plates continues to decrease, and the grain size in these phases becomes less than 300 nm (Fig. 2 f, inset).

Fig. 3 shows the diffraction patterns of the studied alloy in various structural states, as well as the general appearance of the diffraction pattern analysed by the Rietveld method (1 revolution, HPT, 27 °C). The results of qualitative XRD showed that after heat treatment, the Zn, Mg_2Zn_{11}, $FeZn_{13}$ and $MgZn_2$ phases can be identified in the alloy. At the same time, when the alloy is exposed to the HPT method, the general appearance of the diffraction patterns changes significantly (Fig. 3 a). Thus, even after 0.5 revolution of HPT treatment (27 °C), suppression of reflexes corresponding to the $FeZn_{13}$, Mg_2Zn_{11} phases and an increase in reflexes of the Zn phase are observed (Fig. 3 a). In this case, the width of each reflex, especially the Mg_2Zn_{11} phase, increases significantly compared to that characteristic of the initial state (Fig. 3 a). With a further increase in the degree of HPT treatment, the general appearance of the diffraction patterns remains virtually unchanged (Fig. 3 a). However, it should be noted that at high degrees of HPT treatment, a further increase in the width of the reflexes and suppression of the intensity of the reflexes corresponding to the Mg_2Zn_{11} phase are observed.

In the case of HPT treatment at a temperature of 150 °C, an increase in the intensity of the $MgZn_2$ phase reflexes is observed already at the early stages (Fig. 3 a). In this case, the reflexes corresponding to the Zn and Mg_2Zn_{11} phases become wider, as compared to those obtained after HPT at 27 °C. With a further increase in the degree of HPT treatment, an increase in the intensity of the reflexes corresponding to the Zn and $MgZn_2$ phases, and an increase in the width of their peaks are observed.

An example of the diffraction pattern analysis for the alloy state after 1 HPT revolution is shown in Fig. 3 b. It shows the theoretical and experimental diffraction patterns, the difference line and the background line, the difference electron density for the main phase (Zn), and the positions of the reflexes in the form of peak diagrams (Fig. 3 b). It is evident that the change in the difference value ($\rho_{measured}-\rho_{calculated}$) of the electron density of the experiment, and theory for the main phase is extremely insignificant and is contained in a small range of deviations (from −1.35 to +1.35 units) (Fig. 3 b). At the same time, the difference line also has small deviations (Fig. 3 b). These facts indicate a high degree of convergence of the experimental and calculated curves, and this increases the reliability of the data obtained.

Fig. 4 shows the results of the quantitative ratio of the analysed phases depending on the degree of HPT treatment, as well as other characteristics of the microstructure of the main phases. The quantitative XRD data showed that the use of HPT treatment leads, on the one hand, to an increase in the mass fraction of the Zn phase in the alloy, and on the other hand, to the suppression of the content of the Mg_2Z_{n11} and $FeZn_{13}$ phases (Fig. 4 a). Based on the analysis of the width and positions of reflexes in the diffraction pattern, the average size of the CSD, the average dislocation density, and the values of the lattice constant of the main phases were determined.

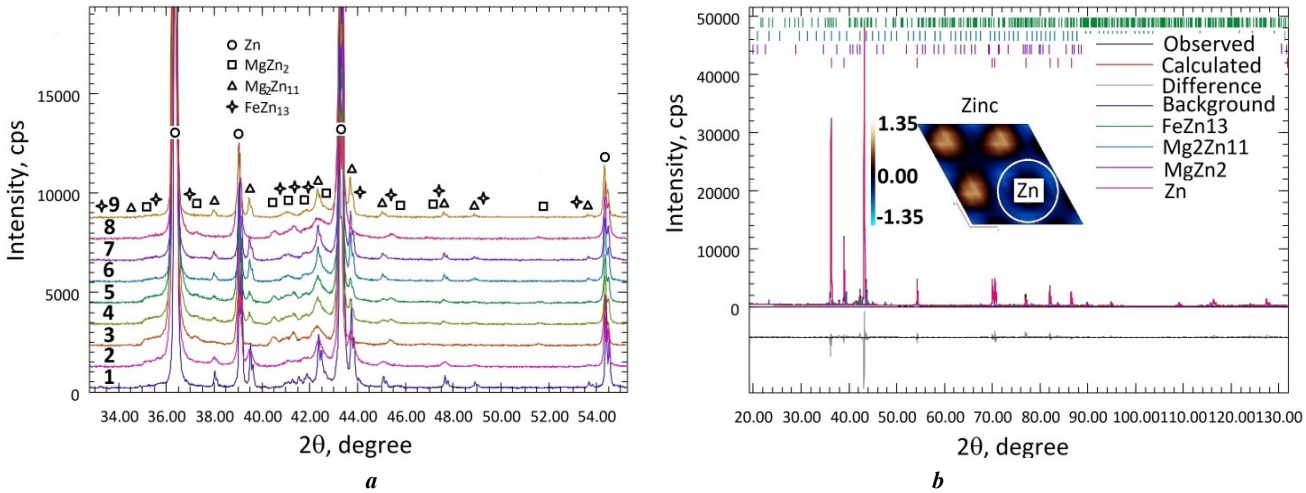

a *b*

Fig. 3. *X-Ray diffraction patterns of the Zn–1%Mg–1%Fe alloy:* ***a*** *– general view of diffraction patterns: 1 – heat treatment; 2 – HPT, 1 rev., 27 °C; 3 – HPT, 1 rev., 150 °C; 4 – HPT, 3 rev., 27 °C; 5 – HPT, 3 rev., 150 °C; 6 – HPT, 6 rev., 27 °C; 7 – HPT, 6 rev., 150 °C; 8 – HPT, 10 rev., 27 °C; 9 – HPT, 10 rev., 150 °C;* ***b*** *– an example of the diffraction pattern processed by the Rietveld method: HPT, 1 rev., 27 °C*

Рис. 3. *Дифрактограммы сплава Zn–1%Mg–1%Fe:* ***a*** *– общий вид дифрактограмм: 1 – термическая обработка; 2 – ИПДК, 1 об., 27 °C; 3 – ИПДК, 1 об., 150 °C; 4 – ИПДК, 3 об., 27 °C; 5 – ИПДК, 3 об., 150 °C; 6 – ИПДК, 6 об., 27 °C; 7 – ИПДК, 6 об., 150 °C; 8 – ИПДК, 10 об., 27 °C; 9 – ИПДК, 10 об., 150 °C;* ***b*** *– пример обработанной методом Ритвельда дифрактограммы: ИПДК, 1 об., 27 °C*

These microstructure characteristics depending on the degree and temperature of HPT treatment are shown in Fig. 4 b–d.

Fig. 5 shows the changes in the crystallographic orientations of grains in the Zn phase depending on the degree and temperature of HPT treatment. For a convenient and visual understanding of the evolution of texture formation processes, the preferred grain orientations in Fig. 5 are shown in the form of an inverse pole figure (IPF) (0001), which is parallel to the plane of the disk (sample). In the initial state of the alloy, the Zn phase grains are characterised by the presence of basic {0001}<1000>, pyramidal {10–11}<0–110> and {21–36}<1–210>, as well as prismatic {21–30}<1–210> and {31–40}<1–320> texture components (Fig. 5). Moreover, compression twin components {11–22}<uwtv> are revealed in some grains (Fig. 5). Analysis of the evolution of the crystallographic texture of Zn phase during HPT showed that the texture formation processes, depending on the degree and temperature of its treatment, have similarities and differences. In particular, even after 1 revolution of HPT at 27 °C, the character of the distribution of texture maxima on the (0001) IPF changes sharply (Fig. 5). In this case, the basic {0001}<1000> texture components are enhanced, while the prismatic {21–30}<1–210> / {31–40}<1–320> and pyramidal {21–36}<1–210> orientations, on the contrary, are suppressed. At the same time, new components {11–21}<1–100>, {20–21}<0–110> and {11–24}<1–100> of pyramidal grain orientations, as well as components {10–12}<uwtv> of tension twinning are formed (Fig. 5).

With an increase in the number of revolutions to 3, the pyramidal, prismatic and twin texture components revealed after 1 HPT revolution are suppressed, and the pole density of the basic component is enhanced (Fig. 5). At high revo-

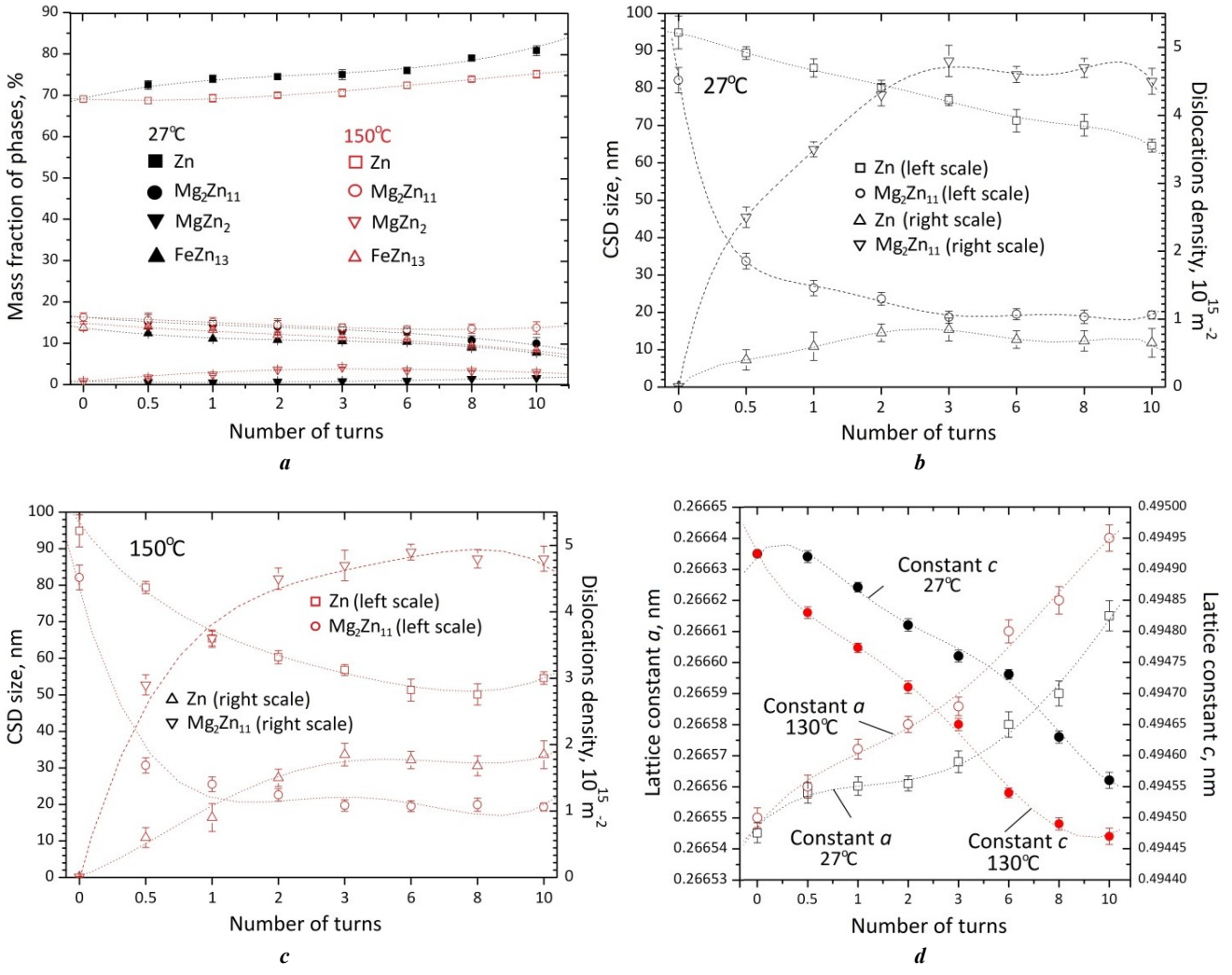

Fig. 4. *Patterns of change in fine structure parameters depending on the number of revolutions of the HPT treatment:* ***a*** *– mass fraction of detected phases;* ***b*** *– average size of coherent scattering domains and average dislocation density at 27 °C;* ***c*** *– average size of coherent scattering domains and average dislocation density at 150 °C;* ***d*** *– lattice constant of Zn*

Рис. 4. *Закономерности изменения параметров тонкой структуры в зависимости от числа оборотов ИПДК-обработки:* ***a*** *– массовой доли обнаруженных фаз;* ***b*** *– усредненного размера областей когерентного рассеяния (ОКР) и средней плотности дислокаций при 27 °C;* ***c*** *– усредненного размера ОКР и средней плотности дислокаций при 150 °C;* ***d*** *– периода решетки Zn*

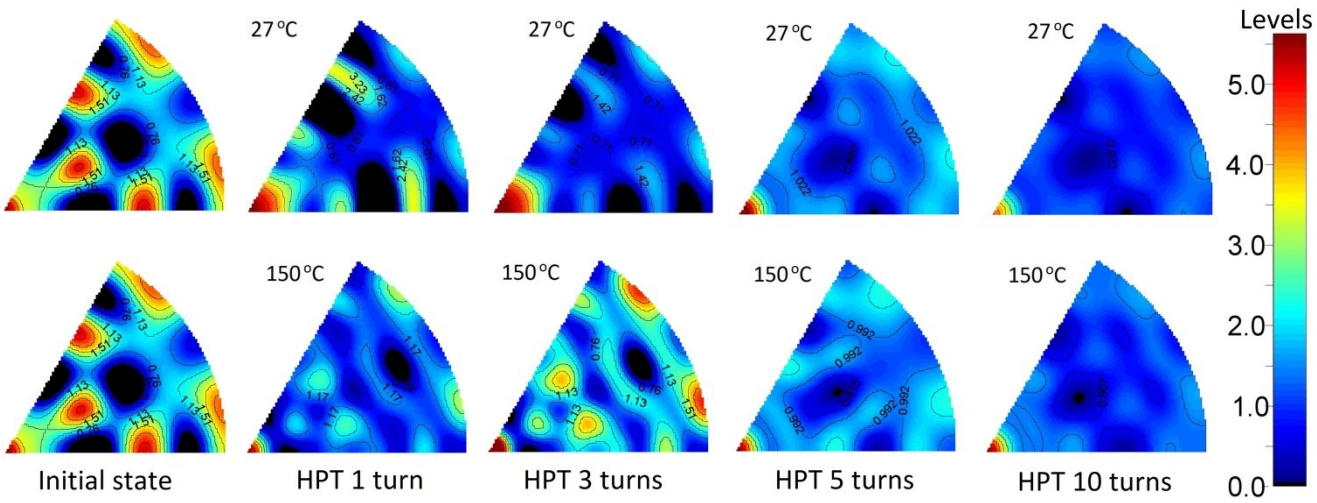

Fig. 5. *Inverse pole figures (0001) for the Zn phase in the initial state and after HPT treatment*
Рис. 5. *Обратные полюсные фигуры (0001) для фазы Zn в исходном состоянии и в состояниях после ИПДК-обработки*

lutions of the HPT treatment, further suppression of all texture components in favor of the basic one is observed, which becomes the main texture component (Fig. 5).

During the HPT treatment of the alloy at a temperature of 150 °C, the evolution of texture formation processes in the Zn phase has its own characteristics. Thus, at the initial stage (1 revolution) of the HPT treatment, compared to that implemented during the HPT at 27 °C, additional texture components are formed (Fig. 5). In particular, new components related to the pyramidal {21–34}<1–210>, {21–36}<1–210> and {31–44}<1–320> types are visible on the IPF (Fig. 5). The pole densities of additional texture components increase with an increase in the number of HPT revolutions to 3 (Fig. 5). In this state, an increase in the basic {000l}<1000> and prismatic {21–30}<1–210> / {31–40}<1–320> texture components is also observed (Fig. 5). At high degrees of HPT treatment, the basic {000l}<1000> texture component predominates over all other components of the crystallographic texture (Fig. 5).

DISCUSSION

The conducted studies have shown that the Zn–1%Mg–1%Fe alloy subjected to HPT treatment demonstrates increased strength characteristics along with sufficient ductility during its extension (Table 1). To determine the reasons for the increase in strength and ductility of this alloy, comprehensive studies of its microstructure were conducted. According to the conducted studies, the initial Zn–Mg–Fe alloy subjected to heat treatment consists of the Zn, Mg_2Zn_{11} and $FeZn_{13}$ phases. In this case, cylindrical $MgZn_2$ particles precipitated in the Mg_2Zn_{11} phase (Fig. 2 a). Earlier, some works [25; 26] also noted that $MgZn_2$ particles strengthening the alloy can precipitate in the Mg_2Zn_{11} phase.

The conducted analysis of the microstructure showed that even at the early stages of HPT treatment (0.5 revolution), the alloy does not exhibit eutectic structures characteristic of the cast state. In this case, a band structure consisting of a mixture of the Zn, $FeZn_{13}$ and Mg_2Zn_{11} phases is formed, in which $MgZn_2$ particles precipitate (Fig. 2 b). $MgZn_2$ particles inside the Mg_2Zn_{11} bands (darker areas) are revealed as numerous light areas of different morphology (Fig. 2 b, inset). According to microscopy data, with an increase in the degree and temperature of HPT treatment, the width of the bands corresponding to the Zn, Mg_2Zn_{11} and $FeZn_{13}$ phases decreases. Moreover, a refinement of the structural components is observed inside the bands of each phase. In particular, the formation of equiaxial grains with a diameter of 230 nm in the Mg_2Zn_{11} bands is demonstrated in the inset to Fig. 2 c. In addition to the structure refinement, at high speeds of HPT treatment, Zn and $MgZn_2$ particles of spherical morphology strengthening the alloy precipitate in the Mg_2Zn_{11} phase (Fig. 2 d, inset). With an increase in the HPT temperature (150 °C), the dynamic strain ageing process is implemented more completely. This fact is explained by an increase in the proportion of $MgZn_2$ particles in the Mg_2Zn_{11} phase (Fig. 4 a). In this regard, one can argue that the role of dispersion, strengthening of the alloy increases significantly with an increase in the HPT temperature.

The obtained microscopy results are in good agreement with the X-ray diffraction analysis data. In particular, the quantitative X-ray diffraction method found that in the initial (as-cast) state of the alloy, the content of the Zn, Mg_2Zn_{11}, $FeZn_{13}$ and $MgZn_2$ phases is 69.0, 17.3, 13.5, and 0.2 %, respectively (Fig. 4 a). According to the literature data [23; 24], the mixture of Zn and Mg_2Zn_{11} phases is in the eutectic state, and this fact is consistent with the SEM study data. At the same time, the presence of the $FeZn_{13}$ phase in the microstructure was also identified as a result of the SEM analysis, and traces of intense precipitation of $MgZn_2$ particles in the Mg_2Zn_{11} phase were observed after heat treatment of the alloy (Fig. 2 a, 3 a).

In the case of HPT treatment, even a small deformation (0.5 revolutions) leads to changes in the ratio of the identified phases. In particular, it is clear that after 0.5 HPT revolution, a regular decrease in the Mg_2Zn_{11} and $FeZn_{13}$ mass fractions is observed (Fig. 4 a). At the same time, the Zn mass fraction increases monotonically (Fig. 4 a). An increase in the degree of deformation leads to a further regular decrease in the content of the Mg_2Zn_{11} and $FeZn_{13}$ phases (Fig. 4 a). At high degrees and an increase in the HPT temperature, the Zn phase content, as well as the $MgZn_2$ (precipitates) mass fraction increase significantly (Fig. 4 a).

As is known [18; 19; 27; 28], metallic materials subjected to HPT are characterised by a grain refinement, an increased density of induced defects, a developed crystallographic texture and an extremely nonequilibrium state of grain boundaries. The XRD analysis of the zinc alloy data shows that the microstructure changes differently in each of the main phases during HPT deformation. In particular, the Mg_2Zn_{11} phase is characterised by a sharp decrease in the CSD size (Fig. 4 b), which can be associated with grain refinement during HPT. It is evident that even at the initial stages of HPT treatment (up to 1 revolution), the average CSD size of the Mg_2Zn_{11} phase decreases to ~30 nm (Fig. 4 b). With an increase in the number of HPT revolutions to 3, a further decrease in the average CSR size down to ~20 nm is observed. At high HPT degrees, the average CSD size in the Mg_2Zn_{11} phase remains virtually unchanged, and remains in the range of 18…22 nm (Fig. 4 b). The same pattern of decrease in the CSD size in the Mg_2Zn_{11} phase is observed, with an increase in the HPT temperature (Fig. 4 c). On the other hand, the process of refinement of the structural elements in the Zn phase during HPT treatment is not as effective as expected (Fig. 4 b). In particular, it is obvious that at the early HPT stages (up to 1 revolution), the average CSD size remains virtually unchanged (Fig. 4 b). Only after reaching high degrees of HPT treatment (after 10 revolutions), the average CSD size in the Zn phase decreases to ~65 nm (Fig. 4 b). On the contrary, with an increase in the HPT temperature to 150 °C, the CSD size of the Zn phase decreases significantly even at the initial stages of deformation (Fig. 4 c). At high degrees of HPT, the CSD size of the Zn phase reaches saturation and is ~50 nm.

Comparative analysis showed, that the average densities of the induced defects in the analysed phases also change non-monotonically (Fig. 4 b). In particular, in the Mg_2Zn_{11} phase, after 3 HPT revolutions, the dislocation density reaches its maximum value ($\sim 4.5 \cdot 10^{15}$ m^{-2}), and then decreases slightly with an increase in the number of revolutions (Fig. 4 b). According to the X-ray diffraction data, a similar trend is observed in the Zn phase. However, compared to the Mg_2Zn_{11} phase, it has a relatively low dislocation density, not exceeding $0.8 \cdot 10^{15}$ m^{-2} (Fig. 4 b). At high degrees of HPT treatment, a decrease in the dislocation density is observed in the Zn phase (Fig. 4 b). With an increase in the HPT temperature to 150 °C, the dislocation density in the Zn phase increases significantly (Fig. 4 c). In this case, in the Mg_2Zn_{11} phase, the dislocation density values found, are comparable with those obtained after HPT at 27 °C (Fig. 4 c).

The changes in the lattice constant values in the Zn phase depending on the degree of HPT treatment shown in Fig. 4 d are interesting. In particular, in the as-cast state, the lattice constant of Zn along the edge *a* of the hexagonal close-packed (hcp) lattice is 0.266549 nm, and along the basic edge *c,* it is 0.494952 nm (Fig. 4 d). The values found differ from the tabular data (a=0.26648 nm, c=0.49467 nm [29]), especially in the direction of the basis *c* of the hcp lattice. After 0.5 revolution of HPT treatment, a gradual increase in the lattice constant along the edge *a,* and a decrease in the value along the *c* direction of the hcp lattice are observed (Fig. 4 d). With a further increase in the number of revolutions and the temperature of HPT, the lattice constant of Zn along the edge *a* continues to increase, and along the face *c* it normally decreases. This change in the Zn lattice constant is most likely associated with the presence of Fe and Mg impurity atoms in this phase, which is supported by the SEM analysis data (Fig. 1 d).

As studies have shown, alloying Zn with Mg and Fe atoms and conducting HPT treatment, made it possible to increase significantly the alloy strength characteristics and simultaneously increase its ductility (Table 1), which meet the requirements for fixing bones and stents. Despite the low tensile strength (33 MPa) of the initial alloy, its microhardness (118 HV) is much higher than that of pure zinc (41 HV according to [1]). As SEM studies have shown, the initial alloy contains coarse Mg_2Zn_{11} and $FeZn_{13}$ phases (Fig. 1). Moreover, according to work [30], the hardness of the Mg_2Zn_{11} phase is ~300 HV and that of the $FeZn_{13}$ phase is 290 HV [31]. In this regard, the high microhardness of the initial alloy can be explained by the presence of coarse Mg_2Zn_{11} and $FeZn_{13}$ phases in its structure. As a result of HPT treatment (e.g. after 1 revolution, 27 °C), the alloy strength increases to 289 MPa, however, the microhardness of the alloy in this state is no more than 114 HV (Table 1). Studies have shown that HPT treatment of the alloy causes both the fragmentation of the Mg_2Zn_{11} and $FeZn_{13}$ phases (Fig. 2), and a decrease in the content of these phases (Fig. 4). At the same time, the proportion of the Zn phase increases (Fig. 4). These facts apparently limit the growth of the alloy microhardness, and explain the observed decrease in its microhardness during HPT. In general, the formation of a band structure consisting of the Zn, $FeZn_{13}$ and Mg_2Zn_{11} phases, grain refinement in the main phases, and the precipitation of particles in them, turned out to be the main factors in the zinc alloy increasing its mechanical properties. An equally important factor determining the level and anisotropy of the strength properties of the alloy under study is its developed crystallographic texture.

Analysis of the crystallographic textures showed that the Zn phase grain orientations in the initial alloy belong to the basic {0001}<1000>, pyramidal {10–11}<0–110> and {21–36}<1–210>, as well as prismatic {21–30}<1–210> and {31–40}<1–320> texture components. At the same time, there are compression twin components {11–22}<uwtv> (Fig. 5). However, when the alloy is subjected to HPT treatment, the spatial orientation of the Zn phase grains in the sample changes significantly, as indicated by the texture maxima redistribution on the (0001) IPF (Fig. 5). In particular, already at the early stages of HPT treatment

(after 1 revolution, 27 °C), suppression of prismatic and pyramidal texture components, and strengthening of the basic orientation of grains are observed. In this case, other orientations of the pyramidal {11–21}<1–100>, {20–21}<0–110> and {11–24}<1–100> types, as well as {10–12}<uwtv> tension twin components are formed (Fig. 5). With an increase in the number of HPT revolutions to 3, the proportion of the basic {0001}<1000> component increases, and all other identified grain orientations are slightly suppressed. At high HPT degrees, further suppression of all texture components is observed in favour of the basic one, which becomes the main one.

With increasing the HPT temperature (150 °C), the texture formation processes proceed identically with the predominance of the basic {0001}<1000> texture component (Fig. 5). However, at the early stages of HPT at 150 °C, except for the components characteristic of HPT at 27 °C, new grain orientations are formed in the sample. In this case, the pole densities of the new texture components increase with an increase in the number of HPT revolutions to 3 (Fig. 5). In this state, the basic {0001}<1000> and prismatic {21–30}<1–210> / {31–40}<1–320> texture components also increase (Fig. 5).

As shown by tensile tests, in the state after 3 revolutions of HPT at 150 °C, the alloy demonstrates the highest mechanical properties (Table 1). In this state, the Zn phase grains have pyramidal, prismatic and twin components of the volume fraction texture, in addition to the basic one. As is known [32; 33], the value of the critical shear stress, which determines the onset of operation of certain slip systems, is minimal for basic systems, and has the highest values for pyramidal, prismatic and twin systems. In this regard, one can argue that the formation of pyramidal, prismatic and twin texture components at the initial stages of HPT treatment of the alloy, contributes to an increase in its strength properties, since their operation requires high loads. At high degrees of HPT, the main orientation is the basic component, and for the operation of the alloy, i. e. for the implementation of its plastic deformation, less impact is required. The formation of a predominantly basic texture component, can explain the decrease in the strength properties of this alloy at high degrees of HPT.

The studies conducted using XRD and microscopy methods showed that as a result of HPT, a unique UFG structure consisting of the Zn, Mg_2Zn_{11} and $FeZn_{13}$ phases, in which particles of spherical morphology precipitate, is formed in the Zn–1%Mg–1%Fe alloy. During HPT, the density of introduced structural defects also increases and a developed crystallographic texture is formed. The discovered facts indicate that dispersion, grain-boundary (according to the Hall–Petch relationship), and dislocation strengthening mechanisms are implemented in the alloy. At the same time, the stability of the pyramidal, prismatic and twin texture components during HPT treatment determine the level and anisotropy of the strength properties of this alloy. In general, compared to pure Zn, the Zn–1%Mg–1%Fe alloy, optimised by the HPT method, exhibits higher strength properties (tensile strength, hardness) with sufficient ductility, and with such characteristics it can be used as implants for some applications [34].

CONCLUSIONS

A new Zn–1%Mg–1%Fe alloy with improved mechanical properties (ultimate tensile strength is 415 MPa, ductility is 82 %) to be used in medicine, as implants, has been produced by alloying and forming a UFG structure in it as a result of HPT (3 revolutions, 150 °C). It has been found that HPT in the main phases (Zn and Mg_2Zn_{11}) results in effective refinement of the grain structure, and an increase in the density of introduced defects. At the initial stages of HPT, a developed crystallographic texture consisting of basic, pyramidal, prismatic and twin texture components is formed in the Zn phase. The stability of the pyramidal, prismatic and twin texture components during HPT, determines the level and anisotropy of the strength properties of this alloy. Effective refinement of grains in the main phases and the formation of the UFG structure, as well as the precipitation of spherical particles with a high content, are the main factors increasing the mechanical properties of this alloy.

REFERENCES

1. García-Mintegui C., Córdoba L.C., Buxadera-Palomero J., Marquina A., Jiménez-Piqué E., Ginebra M.-P., Cortina J.L., Pegueroles M. Zn-Mg and Zn-Cu alloys for stenting applications: From nanoscale mechanical characterization to in vitro degradation and biocompatibility. *Bioactive Materials*, 2021, vol. 6, no. 12, pp. 4430–4446. DOI: 10.1016/j.bioactmat.2021.04.015.
2. Wei Yuan, Dandan Xia, Shuilin Wu, Yufeng Zheng, Zhenpeng Guan, Rau J.V. A review on current research status of the surface modification of Zn-based biodegradable metals. *Bioactive Materials*, 2022, vol. 7, pp. 192–216. DOI: 10.1016/j.bioactmat.2021.05.018.
3. Wątroba M., Mech K., Bednarczyk W., Kawałko J., Marciszko-Wiąckowska M., Marzec M., Shepherd D.E.T., Bała P. Long-term in vitro corrosion behavior of Zn-3Ag and Zn-3Ag-0.5Mg alloys considered for biodegradable implant applications. *Materials & Design*, 2022, vol. 213, article number 110289. DOI: 10.1016/j.matdes.2021.110289.
4. Huang Tian, Liu Zhilin, Wu Dachao, Yu Hailiang. Microstructure, mechanical properties, and biodegradation response of the grain-refined Zn alloys for potential medical materials. *Journal of materials research and technology*, 2021, vol. 15, pp. 226–240. DOI: 10.1016/j.jmrt.2021.08.024.
5. Young J., Reddy R.G. Synthesis, mechanical properties, and in vitro corrosion behavior of biodegradable Zn–Li–Cu alloys. *Journal of Alloys and Compounds*, 2020, vol. 844, article number 156257. DOI: 10.1016/j.jallcom.2020.156257.
6. Zhuo Xiaoru, Wu Yuna, Ju Jia, Liu Huan, Jiang Jinghua, Hu Zhichao, Bai Jing, Xue Feng. Recent progress of novel biodegradable zinc alloys: from the perspective of strengthening and toughening. *Journal of Materials Research and Technology*, 2022, vol. 17, pp. 244–269. DOI: 10.1016/j.jmrt.2022.01.004.
7. Shao Xiaoxi, Wang Xiang, Xu Fangfang et al. In vivo biocompatibility and degradability of a Zn-Mg-Fe alloy osteosynthesis system. *Bioactive Materials*, 2021, vol. 7, pp. 154–166. DOI: 10.1016/j.bioactmat.2021.05.012.

8. Su Yingchao, Fu Jiayin, Lee Wonsae, Du Shaokang, Qin Yi-Xian, Zheng Yufeng, Wang Yadong, Zhu Donghui. Improved mechanical, degradation, and biological performances of Zn-Fe alloys as bioresorbable implants. *Bioactive Materials*, 2022, vol. 17, pp. 334–343. DOI: 10.1016/j.bioactmat.2021.12.030.
9. He Jin, Li Da-Wei, He Feng-Li et al. A study of degradation behaviour and biocompatibility of Zn-Fe alloy prepared by electrodeposition. *Materials Science and Engineering: C*, 2020, vol. 117, article number 111295. DOI: 10.1016/j.msec.2020.111295.
10. Oliver A.A., Guillory R.J., Flom K.L., Morath L.M., Kolesar T.M., Mostaed E., Sikora-Jasinska M., Drelich J.W., Goldman J. Analysis of vascular inflammation against bioresorbable Zn-Ag based alloys. *ACS Applied Bio Materials*, 2020, vol. 3, no. 10, pp. 6779–6789. DOI: 10.1021/acsabm.0c00740.
11. Kafri A., Ovadia S., Goldman J., Drelich J., Aghion E. The Suitability of Zn–1.3%Fe Alloy as a Biodegradable Implant Material. *Metals*, 2018, vol. 8, no. 3, article number 153. DOI: 10.3390/met8030153.
12. Shi Zhang-Zhi, Gao Xi-Xian, Chen Hong-Ting, Liu Xue-Feng, Li Ang, Zhang Hai-Jun, Wang Lu-Ning. Enhancement in mechanical and corrosion resistance properties of a biodegradable Zn-Fe alloy through second phase refinement. *Materials Science and Engineering: C*, 2020, vol. 116, article number 111197. DOI: 10.1016/j.msec.2020.111197.
13. Shiyang Liu, Kent D., Doan Nghiem, Dargusch M., Gui Wang. Effects of deformation twinning on the mechanical properties of biodegradable Zn-Mg alloys. *Bioactive Materials*, 2019, vol. 4, pp. 8–16. DOI: 10.1016/j.bioactmat.2018.11.001.
14. Galib R.H., Sharif A. Development of Zn-Mg alloys as a degradable biomaterial. *Advances in Alloys and Compounds*, 2015, vol. 1, no. 1, pp. 1–7.
15. Vojtech D., Kubasek J., Serak J., Novak P. Mechanical and corrosion properties of newly developed biodegradable Zn based alloys for bone fixation. *Acta Biomaterialia*, 2011, vol. 7, no. 9, pp. 3515–3522. DOI: 10.1016/j.actbio.2011.05.008.
16. Li Huafang, Xie Xin-Hui, Zheng Yufeng et al. Development of biodegradable Zn-1X binary alloys with nutrient alloying elements Mg, Ca and Sr. *Scientific Reports*, 2015, vol. 5, article number 10719. DOI: 10.1038/srep10719.
17. Xue Penghao, Ma Minglong, Li Yongjun, Li Xinggang, Yuan Jiawei, Shi Guoliang, Wang Kaikun, Zhang Kui. Microstructure, Mechanical Properties, and in Vitro Corrosion Behavior of Biodegradable Zn-1Fe-xMg Alloy. *Materials*, 2020, vol. 13, no. 21, article number 4835. DOI: 10.3390/ma13214835.
18. Valiev R.Z., Islamgaliev R.K., Alexandrov I.V. Bulk nanostructured materials from severe plastic deformation. *Progress in Materials Science*, 2000, vol. 45, no. 2, pp. 103–189. DOI: 10.1016/S0079-6425(99)00007-9.
19. Sitdikov V.D., Khafizova E.D., Polenok M.V. Microstructure and properties of the Zn–1%Li–2%Mg alloy subjected to severe plastic deformation. *Frontier Materials & Technologies*, 2023, no. 2, pp. 117–130. DOI: 10.18323/2782-4039-2023-2-64-7.
20. Luqman M., Ali Y., Zaghloul M.M.Y., Sheikh F.A., Chan V., Abdal-hay A. Grain Refinement Mechanism and its effect on Mechanical Properties and Biodegradation Behaviors of Zn Alloys – A Review. *Journal of Materials Research and Technology*, 2023, vol. 24, pp. 7338–7365. DOI: 10.1016/j.jmrt.2023.04.219.
21. Leoni M., Confente T., Scardi P. PM2K: A flexible program implementing Whole Powder Pattern Modelling. *Zeitschrift für Kristallographie, Supplement*, 2006, vol. 1, no. 23, pp. 249–254.
22. Rietveld H.M. A profile refinement method for nuclear and magnetic structures. *Journal of Applied Crystallography*, 1969, vol. 2, no. 2, pp. 65–71. DOI: 10.1107/S0021889869006558.
23. Pingli Jiang, Blawert C., Zheludkevich M.L. The Corrosion Performance and Mechanical Properties of Mg-Zn Based Alloys – A Review. *Corrosion and Materials Degradation*, 2020, vol. 1, no. 1, pp. 92–158. DOI: 10.3390/cmd1010007.
24. Shi Zhang-Zhi, Gao Xi-Xian, Zhang Hai-Jun, Liu Xue-Feng, Li Hui-Yan, Zhou Chao, Yin Xu-Xia, Wang Lu-Ning. Design biodegradable Zn alloys: Second phases and their significant influences on alloy properties. *Bioactive Materials*, 2020, vol. 5, no. 2, pp. 210–218. DOI: 10.1016/j.bioactmat.2020.02.010.
25. Ye Lifeng, Huang He, Sun Chao et al. Effect of grain size and volume fraction of eutectic structure on mechanical properties and corrosion behavior of as-cast Zn-Mg binary alloys. *Journal of Materials Research and Technology*, 2021, vol. 16, pp. 1673–1685. DOI: 10.1016/j.jmrt.2021.12.101.
26. Huang He, Liu Huan, Wang Lisha, Yan Kai, Li Yuhua, Jiang Jinghua, Ma Aibin, Xue Feng, Bai Jing. Revealing the effect of minor Ca and Sr additions on microstructure evolution and mechanical properties of Zn-0.6 Mg alloy during multi-pass equal channel angular pressing. *Journal of Alloys and Compounds*, 2020, vol. 844, article number 155923. DOI: 10.1016/j.jallcom.2020.155923.
27. Sitdikov V.D., Kulyasova O.B., Sitdikova G.F., Islamgaliev R.K., Yufeng Zheng. Structural-phase transformations in the Zn-Li-Mg alloy exposed to the severe plastic torsion deformation. *Frontier Materials & Technologies,* 2022, no. 3-2, pp. 44–55. DOI: 10.18323/2782-4039-2022-3-2-44-55.
28. Nazarov A.A. Nonequilibrium grain boundaries in bulk nanostructured metals and their recovery under the influences of heating and cyclic deformation. Review. *Letters on materials*, 2018, vol. 8, no. 3, pp. 372–381. DOI: 10.22226/2410-3535-2018-3-372-381.
29. Wyckoff R.W.G. Hexagonal closest packed, hcp, structure. *Crystal Structures*. New York, Interscience Publishers Publ., 1963. Vol. 1, pp. 7–83.
30. Necas D., Marek I., Pinc J., Vojtech D., Kubásek J. Advanced Zinc–Magnesium Alloys Prepared by Mechanical Alloying and Spark Plasma Sintering. *Materials*, 2022, vol. 15, no. 15, article number 5272. DOI: 10.3390/ma15155272.
31. Han Kwangsik, Lee Inho, Ohnuma I., Okuda K., Kainuma R. Micro-Vickers Hardness of Intermetallic Compounds in the Zn-rich Portion of Zn–Fe Binary System. *ISIJ International*, 2018, vol. 58, no. 9, pp. 1578–1583. DOI: 10.2355/isijinternational.ISIJINT-2018-111.
32. Liu Shiyang, Kent D., Zhan Hongyi, Doan Nghiem, Dargusch M., Wang Gui. Dynamic recrystallization of

pure zinc during high strain-rate compression at ambient temperature. *Materials Science and Engineering: A*, 2020, vol. 784, article number 139325. DOI: 10.1016/j.msea.2020.139325.
33. Pham Nguyen, Abbès F., Lecomte J.S., Schuman C., Abbès B. Inverse Identification of Single-Crystal Plasticity Parameters of HCP Zinc from Nanoindentation Curves and Residual Topographies. *Nanomaterials (Basel)*, 2022, vol. 12, no. 3, article number 300. DOI: 10.3390/nano12030300.
34. Yang Hongtao, Qu Xinhua, Lin Wenjiao, Chen Dafu, Zhu Donghui, Dai Kerong, Zheng Yufeng. Enhanced osseointegration of Zn-Mg composites by tuning the release of Zn ions with sacrificial Mg rich anode design. *ACS Biomaterials Science & Engineering*, 2018, vol. 5, no. 2, pp. 453–467. DOI: 10.1021/acsbiomaterials.8b01137.

СПИСОК ЛИТЕРАТУРЫ

1. García-Mintegui C., Córdoba L.C., Buxadera-Palomero J., Marquina A., Jiménez-Piqué E., Ginebra M.-P., Cortina J.L., Pegueroles M. Zn-Mg and Zn-Cu alloys for stenting applications: From nanoscale mechanical characterization to in vitro degradation and biocompatibility // Bioactive Materials. 2021. Vol. 6. № 12. P. 4430–4446. DOI: 10.1016/j.bioactmat.2021.04.015.
2. Yuan Wei, Xia Dandan, Wu Shuilin, Zheng Yufeng, Guan Zhenpeng, Rau J.V. A review on current research status of the surface modification of Zn-based biodegradable metals // Bioactive Materials. 2022. Vol. 7. P. 192–216. DOI: 10.1016/j.bioactmat.2021.05.018.
3. Wątroba M., Mech K., Bednarczyk W., Kawałko J., Marciszko-Wiąckowska M., Marzec M., Shepherd D.E.T., Bała P. Long-term in vitro corrosion behavior of Zn-3Ag and Zn-3Ag-0.5Mg alloys considered for biodegradable implant applications // Materials & Design. 2022. Vol. 213. Article number 110289. DOI: 10.1016/j.matdes.2021.110289.
4. Huang Tian, Liu Zhilin, Wu Dachao, Yu Hailiang. Microstructure, mechanical properties, and biodegradation response of the grain-refined Zn alloys for potential medical materials // Journal of materials research and technology. 2021. Vol. 15. P. 226–240. DOI: 10.1016/j.jmrt.2021.08.024.
5. Young J., Reddy R.G. Synthesis, mechanical properties, and in vitro corrosion behavior of biodegradable Zn–Li–Cu alloys // Journal of Alloys and Compounds. 2020. Vol. 844. Article number 156257. DOI: 10.1016/j.jallcom.2020.156257.
6. Zhuo Xiaoru, Wu Yuna, Ju Jia, Liu Huan, Jiang Jinghua, Hu Zhichao, Bai Jing, Xue Feng. Recent progress of novel biodegradable zinc alloys: from the perspective of strengthening and toughening // Journal of Materials Research and Technology. 2022. Vol. 17. P. 244–269. DOI: 10.1016/j.jmrt.2022.01.004.
7. Shao Xiaoxi, Wang Xiang, Xu Fangfang et al. In vivo biocompatibility and degradability of a Zn-Mg-Fe alloy osteosynthesis system // Bioactive Materials. 2021. Vol. 7. P. 154–166. DOI: 10.1016/j.bioactmat.2021.05.012.
8. Su Yingchao, Fu Jiayin, Lee Wonsae, Du Shaokang, Qin Yi-Xian, Zheng Yufeng, Wang Yadong, Zhu Donghui. Improved mechanical, degradation, and biological performances of Zn-Fe alloys as bioresorbable implants // Bioactive Materials. 2022. Vol. 17. P. 334–343. DOI: 10.1016/j.bioactmat.2021.12.030.
9. He Jin, Li Da-Wei, He Feng-Li et al. A study of degradation behaviour and biocompatibility of Zn-Fe alloy prepared by electrodeposition // Materials Science and Engineering: C. 2020. Vol. 117. Article number 111295. DOI: 10.1016/j.msec.2020.111295.
10. Oliver A.A., Guillory R.J., Flom K.L., Morath L.M., Kolesar T.M., Mostaed E., Sikora-Jasinska M., Drelich J.W., Goldman J. Analysis of vascular inflammation against bioresorbable Zn-Ag based alloys // ACS Applied Bio Materials. 2020. Vol. 3. № 10. P. 6779–6789. DOI: 10.1021/acsabm.0c00740.
11. Kafri A., Ovadia S., Goldman J., Drelich J., Aghion E. The Suitability of Zn–1.3%Fe Alloy as a Biodegradable Implant Material // Metals. 2018. Vol. 8. № 3. Article number 153. DOI: 10.3390/met8030153.
12. Shi Zhang-Zhi, Gao Xi-Xian, Chen Hong-Ting, Liu Xue-Feng, Li Ang, Zhang Hai-Jun, Wang Lu-Ning. Enhancement in mechanical and corrosion resistance properties of a biodegradable Zn-Fe alloy through second phase refinement // Materials Science and Engineering: C. 2020. Vol. 116. Article number 111197. DOI: 10.1016/j.msec.2020.111197.
13. Liu Shiyang, Kent D., Doan Nghiem, Dargusch M., Wang Gui. Effects of deformation twinning on the mechanical properties of biodegradable Zn-Mg alloys // Bioactive Materials. 2019. Vol. 4. P. 8–16. DOI: 10.1016/j.bioactmat.2018.11.001.
14. Galib R.H., Sharif A. Development of Zn-Mg alloys as a degradable biomaterial // Advances in Alloys and Compounds. 2015. Vol. 1. № 1. P. 1–7.
15. Vojtech D., Kubasek J., Serak J., Novak P. Mechanical and corrosion properties of newly developed biodegradable Zn based alloys for bone fixation // Acta Biomaterialia. 2011. Vol. 7. № 9. P. 3515–3522. DOI: 10.1016/j.actbio.2011.05.008.
16. Li Huafang, Xie Xin-Hui, Zheng Yufeng et al. Development of biodegradable Zn-1X binary alloys with nutrient alloying elements Mg, Ca and Sr // Scientific Reports. 2015. Vol. 5. Article number 10719. DOI: 10.1038/srep10719.
17. Xue Penghao, Ma Minglong, Li Yongjun, Li Xinggang, Yuan Jiawei, Shi Guoliang, Wang Kaikun, Zhang Kui. Microstructure, Mechanical Properties, and in Vitro Corrosion Behavior of Biodegradable Zn-1Fe-xMg Alloy // Materials. 2020. Vol. 13. № 21. Article number 4835. DOI: 10.3390/ma13214835.
18. Valiev R.Z., Islamgaliev R.K., Alexandrov I.V. Bulk nanostructured materials from severe plastic deformation // Progress in Materials Science. 2000. Vol. 45. № 2. P. 103–189. DOI: 10.1016/S0079-6425(99)00007-9.
19. Ситдиков В.Д., Хафизова Э.Д., Поленок М.В. Микроструктура и свойства сплава Zn–1%Li–2%Mg, подвергнутого интенсивной пластической деформации // Frontier Materials & Technologies. 2023. № 2. С. 117–130. DOI: 10.18323/2782-4039-2023-2-64-7.
20. Luqman M., Ali Y., Zaghloul M.M.Y., Sheikh F.A., Chan V., Abdal-hay A. Grain Refinement Mechanism and its effect on Mechanical Properties and Biodegradation Behaviors of Zn Alloys – A Review // Journal of

Materials Research and Technology. 2023. Vol. 24. P. 7338–7365. DOI: 10.1016/j.jmrt.2023.04.219.
21. Leoni M., Confente T., Scardi P. PM2K: A flexible program implementing Whole Powder Pattern Modelling // Zeitschrift für Kristallographie, Supplement. 2006. Vol. 1. № 23. P. 249–254.
22. Rietveld H.M. A profile refinement method for nuclear and magnetic structures // Journal of Applied Crystallography. 1969. Vol. 2. № 2. P. 65–71. DOI: 10.1107/S0021889869006558.
23. Jiang Pingli, Blawert C., Zheludkevich M.L. The Corrosion Performance and Mechanical Properties of Mg-Zn Based Alloys – A Review // Corrosion and Materials Degradation. 2020. Vol. 1. № 1. P. 92–158. DOI: 10.3390/cmd1010007.
24. Shi Zhang-Zhi, Gao Xi-Xian, Zhang Hai-Jun, Liu Xue-Feng, Li Hui-Yan, Zhou Chao, Yin Xu-Xia, Wang Lu-Ning. Design biodegradable Zn alloys: Second phases and their significant influences on alloy properties // Bioactive Materials. 2020. Vol. 5. № 2. P. 210–218. DOI: 10.1016/j.bioactmat.2020.02.010.
25. Ye Lifeng, Huang He, Sun Chao et al. Effect of grain size and volume fraction of eutectic structure on mechanical properties and corrosion behavior of as-cast Zn-Mg binary alloys // Journal of Materials Research and Technology. 2021. Vol. 16. P. 1673–1685. DOI: 10.1016/j.jmrt.2021.12.101.
26. Huang He, Liu Huan, Wang Lisha, Yan Kai, Li Yuhua, Jiang Jinghua, Ma Aibin, Xue Feng, Bai Jing. Revealing the effect of minor Ca and Sr additions on microstructure evolution and mechanical properties of Zn-0.6 Mg alloy during multi-pass equal channel angular pressing // Journal of Alloys and Compounds. 2020. Vol. 844. Article number 155923. DOI: 10.1016/j.jallcom.2020.155923.
27. Ситдиков В.Д., Кулясова О.Б., Ситдикова Г.Ф., Исламгалиев Р.К., Юфенг Ж. Структурно-фазовые превращения в Zn–Li–Mg сплаве, подвергнутом интенсивной пластической деформации кручением // Frontier Materials & Technologies. 2022. № 3-2. С. 44–55. DOI: 10.18323/2782-4039-2022-3-2-44-55.
28. Nazarov A.A. Nonequilibrium grain boundaries in bulk nanostructured metals and their recovery under the influences of heating and cyclic deformation. Review // Letters on materials. 2018. Vol. 8. № 3. P. 372–381. DOI: 10.22226/2410-3535-2018-3-372-381.
29. Wyckoff R.W.G. Hexagonal closest packed, HCP, structure // Crystal Structures. New York: Interscience Publishers, 1963. Vol. 1. P. 7–83.
30. Necas D., Marek I., Pinc J., Vojtech D., Kubásek J. Advanced Zinc–Magnesium Alloys Prepared by Mechanical Alloying and Spark Plasma Sintering // Materials. 2022. Vol. 15. № 15. Article number 5272. DOI: 10.3390/ma15155272.
31. Han Kwangsik, Lee Inho, Ohnuma I., Okuda K., Kainuma R. Micro-Vickers Hardness of Intermetallic Compounds in the Zn-rich Portion of Zn–Fe Binary System // ISIJ International. 2018. Vol. 58. № 9. P. 1578–1583. DOI: 10.2355/isijinternational.ISIJINT-2018-111.
32. Liu Shiyang, Kent D., Zhan Hongyi, Doan Nghiem, Dargusch M., Wang Gui. Dynamic recrystallization of pure zinc during high strain-rate compression at ambient temperature // Materials Science and Engineering: A. 2020. Vol. 784. Article number 139325. DOI: 10.1016/j.msea.2020.139325.
33. Nguyen Pham, Abbès F., Lecomte J.S., Schuman C., Abbès B. Inverse Identification of Single-Crystal Plasticity Parameters of HCP Zinc from Nanoindentation Curves and Residual Topographies // Nanomaterials (Basel). 2022. Vol. 12. № 3. Article number 300. DOI: 10.3390/nano12030300.
34. Yang Hongtao, Qu Xinhua, Lin Wenjiao, Chen Dafu, Zhu Donghui, Dai Kerong, Zheng Yufeng. Enhanced osseointegration of Zn-Mg composites by tuning the release of Zn ions with sacrificial Mg rich anode design // ACS Biomaterials Science & Engineering. 2018. Vol. 5. № 2. P. 453–467. DOI: 10.1021/acsbiomaterials.8b01137.

Микроструктура, кристаллографическая текстура и механические свойства сплава Zn–1%Mg–1%Fe, подвергнутого интенсивной пластической деформации

Ситдиков Виль Даянович*[1,2,4], доктор физико-математических наук,
старший эксперт, старший научный сотрудник
Хафизова Эльвира Динифовна[2,3,5], кандидат технических наук,
доцент кафедры материаловедения и физики металлов,
старший научный сотрудник НИЛ «Металлы и сплавы при экстремальных воздействиях»
Поленок Милена Владиславовна[2,3,6], магистрант кафедры материаловедения и физики металлов,
лаборант НИЛ «Металлы и сплавы при экстремальных воздействиях»
[1]*ООО «РН-БашНИПИнефть», Уфа (Россия)*
[2]*Институт физики молекул и кристаллов Уфимского федерального исследовательского центра РАН, Уфа (Россия)*
[3]*Уфимский университет науки и технологий, Уфа (Россия)*

***E-mail:** SitdikovVD@bnipi.rosneft.ru

[4]ORCID: https://orcid.org/0000-0002-9948-1099
[5]ORCID: https://orcid.org/0000-0002-4618-412X
[6]ORCID: https://orcid.org/0000-0001-9774-1689

Поступила в редакцию 09.02.2024 *Принята к публикации 19.07.2024*

Аннотация: Статья посвящена получению, анализу микроструктуры, кристаллографической текстуры и механизмов деформации ультрамелкозернистого (УМЗ) цинкового Zn–1%Mg–1%Fe сплава, демонстрирующего уникальные физико-механические свойства по сравнению с его крупнокристаллическими аналогами. Цинковый сплав с улучшенными механическими свойствами разрабатывали в два этапа. На первом этапе на основе анализа литературных данных отливали сплав со следующим химическим составом: Zn–1%Mg–1%Fe. В дальнейшем сплав подвергали интенсивной пластической деформации кручением (ИПДК) с целью повышения механических свойств в результате измельчения зеренной структуры и реализации в нем динамического деформационного старения. Проведенные механические испытания на растяжения образцов и оценка твердости сплава показали, что ИПДК-обработка приводит к росту предела его прочности до 415 МПа, увеличению твердости до значения 144 HV и повышению пластичности до 82 %. Полученные механические характеристики демонстрируют пригодность использования разработанного сплава в медицине в качестве некоторых имплантатов (стентов), требующих больших приложенных нагрузок. Для объяснения причин повышения механических свойств данного сплава проведены комплексные испытания методами микроскопии и рентгеноструктурного анализа. Анализ микроструктуры показал, что при формировании УМЗ структуры реализуется фазовый переход по следующей схеме: $Zn_{эвтектика} + Mg_2Zn_{11эвтектика} + FeZn_{13} \rightarrow Zn_{фаза} + Mg_2Zn_{11фаза} + MgZn_{2частицы} + Zn_{частицы}$. Установлено, что в результате ИПДК-обработки в основных фазах (Zn, Mg_2Zn_{11}) происходит измельчение зеренной структуры, повышение плотности внесенных дефектов и формирование развитой кристаллографической текстуры, состоящей из базисных, пирамидальных, призматических и двойниковых компонент текстуры. Показано, что стойкость пирамидальных, призматических и двойниковых компонент текстуры на начальных этапах ИПДК определяет уровень и анизотропию прочностных свойств данного сплава. Обсуждается взаимосвязь обнаруженных структурных особенностей полученного сплава с его уникальными механическими свойствами.

Ключевые слова: сплав Zn–1%Mg–1%Fe; фазовые переходы в цинковом сплаве; интенсивная пластическая деформация; методы рентгеновского рассеяния; механические свойства; прочность; пластичность; кристаллографическая текстура.

Благодарности: Исследование выполнено за счет гранта Российского научного фонда № 23-29-00667, https://rscf.ru/project/23-29-00667.

Для цитирования: Ситдиков В.Д., Хафизова Э.Д., Поленок М.В. Микроструктура, кристаллографическая текстура и механические свойства сплава Zn–1%Mg–1%Fe, подвергнутого интенсивной пластической деформации // Frontier Materials & Technologies. 2024. № 3. С. 75–88. DOI: 10.18323/2782-4039-2024-3-69-7.